Scripta Materialia 127 (2017) 151–155

Contents lists available at ScienceDirect

Scripta Materialia

journal homepage: www.elsevier.com/locate/scriptamat

Regular Article

Local flow stresses in interpenetrating-phase composites based on nanoporous gold — *In situ* diffraction

Ke Wang [a,*], Christian Hartig [a], Malte Blankenburg [b], Martin Müller [b], Robert Günther [a], Jörg Weissmüller [a]

[a] Institute of Materials Physics and Technology, Hamburg University of Technology, Hamburg, Germany
[b] Institute of Materials Research, Helmholtz-Zentrum Geesthacht, Geesthacht, Germany

ARTICLE INFO

Article history:
Received 17 July 2016
Received in revised form 16 September 2016
Accepted 18 September 2016
Available online 23 September 2016

Keywords:
Nanoporous gold
Composites
X-ray diffraction
Local stress
Small-scale plasticity

ABSTRACT

We report a synchrotron *in situ* diffraction experiment exploring stress evolution during compression of interpenetrating-phase nanocomposites based on nanoporous gold and polymer. While previous experiments provided indirect indication of local flow conditions based on macroscopic effective flow stress and micromechanics models such as Gibson-Ashby scaling law, the lattice parameter data of our experiment access the flow stress directly. At small structure size we find excellent agreement with previous reports, supporting the match between material and model of those studies. Yet, deviations at larger structure size suggest that coarsening generates defects in metal network structure that are ignored by standard models.

The micro- and nanostructure of nanoporous gold (NPG) prepared by dealloying can be described as a polycrystal with a grain size of 50–200 μm, where each grain consists of interconnected ligaments of characteristic size $L = 20$–150 nm [1–3]. All ligaments in a grain share a common crystal lattice. Owing to their small size, along with the trend of smaller is stronger [4–7], the ligaments exhibit a high local strength. In order to exploit this strength in an engineering material, composites have been proposed which achieve interesting values of strength and ductility; they are made by infiltration of NPG with polymers. First results showed a distinct increase of yield stress and ductility for NPG which was infiltrated with epoxy or polyurethane [8,9]. A micromechanic iso-strain model predicts the stress in the strong Au phase in good agreement with independent observations of the yielding of porous metal bodies without polymer [9,10]. Yet, a direct confirmation of the acting stress and of the local yield strength is desirable. Here, we report results of an *in situ* synchrotron experiment measuring the stress in the ligaments directly from the Au lattice parameters during plastic flow.

A considerable interest has centred on NPG as a model system for small-scale plasticity, and this adds relevance to our study. Systematic variations of strength with ligament size have been reported by several groups, yet the magnitude of the strength and the size exponent are controversial. The deviations may connect to the quite different experimental approaches, micropillar- [6,11] and nanoindentation testing [1, 11–14] *versus* classic mm-scale compression [2,9,10] or even tension [15] tests. Furthermore, the translation from macroscopic to microscopic behavior almost universally rests on the Gibson-Ashby scaling equations [16] for foams. These equations do not strictly apply to the high solid fraction at hand, and they ignore possible defects in the network structure that may take the form of disconnected ligaments [10,17]. Our direct investigation of the acting flow stress is free of these uncertainties and may thus verify the indirect analysis in the existing literature.

Cylindrical samples of NPG, 1.1 mm in diameter and 1.6 mm long, were prepared by following the procedures in Ref. [9]. The master alloy $Au_{25}Ag_{75}$ was prepared by arc-melting, homogenized by annealing for 100 h at 850 °C, shaped by wire drawing and cutting with a wire saw and finally annealed in vacuum during 3 h at 650 °C for recovery. Dealloying at ambient temperature used 1 M $HClO_4$ prepared from $HClO_4$ (Suprapur R, Merck) and ultrapure water (18.2 M cm) at potential of 0.75 V *versus* an Ag/AgCl pseudo-reference electrode in the same solution (+0.202 V *vs.* Ag/AgCl in saturated KCl). After the current decreased to below 10 μA, an increase of the applied potential to 0.85 V for 3 h led to a completion of dealloying. Samples were rinsed in ultrapure water and dried in vacuum for 3 days. Subsequent annealing at 300 °C in air for or 2 or 30 min served to increase the mean ligament size. The composites were prepared in a vacuum impregnation unit (CitoVaca, Struers). Molds containing dry NPG were evacuated and then filled *in situ* with a mixture of bisphenol F epoxy resin and amine hardener, see Ref. [9] for details. For brevity, we designate the used epoxy resin as BE. The molds were then heated to 60 °C for 20 min in

* Corresponding author.
E-mail address: k.wang@tu-harburg.de (K. Wang).

http://dx.doi.org/10.1016/j.scriptamat.2016.09.026

air to accelerate curing. Surplus polymer was subsequently removed by lifting the sample out of the polymer and blotting with a tissue. A second heating at 60 °C for 48 h completed the curing.

A scanning electron microscope (SEM; LEO 1530 Gemini) operated at 10 kV was used for characterizing the microstructure. Polished surfaces of the composite sample for SEM analysis were prepared by cutting and wet grinding. At least 20 measurements of the smallest projected ligament diameter were taken on the as-polished cross-sectional surface. The results are 60 ± 12 nm for our sample with 2 min annealing and 200 ± 25 nm for the one with 30 min annealing. We refer to those two samples by NC_{60} and NC_{200}, respectively. Solid fractions, φ, of samples made under identical conditions have been explored previously [8], and specifically $\varphi = 0.29$ and 0.42 for sample NC_{60} and NC_{200}, respectively.

In situ X-ray diffraction investigated one sample for each of the two ligament sizes. We used the EH1 end station of the beam line P07 at PETRA III, with an X-ray energy $E = 87.4$ keV [18]. A Perkin Elmer 1621 flat panel detector, 1538 mm distant from the samples, registered the 2D-scattering pattern *in situ* during the compression tests. The beam size on the sample was 0.4×0.4 mm^2 and the exposure time was 2 s. Fig. 1(A) shows the geometry of the diffraction. The initial reference state was an external stress of 20 MPa in order to discard artefacts from sample movement during the initial loading.

The mechanical tests used an *in situ* compression device equipped with a load cell. Strain was determined from the load surface displacement. Constant engineering strain rates of 1.5×10^{-4} s^{-1} and 1.9×10^{-4} s^{-1} were applied for specimens NC_{60} and NC_{200}, respectively. The true compression stress, σ_t, was calculated under the assumption of constant volume, $\sigma_t = F(1-|\varepsilon_p|)/A_0$ where A_0 is the initial cross section and F, ε_p are the load and the plastic strain.

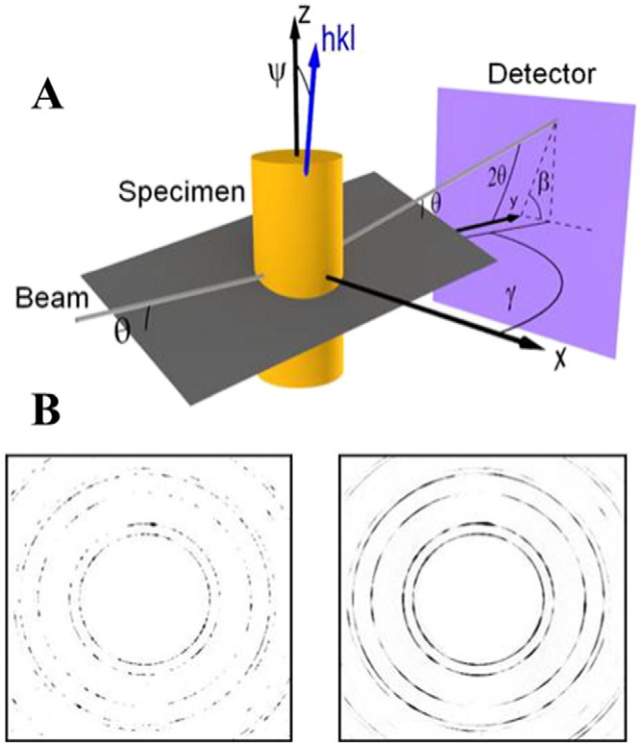

Fig. 1. (A) Schematic illustration of diffraction geometry, showing cylindrical sample (golden) aligned with Cartesian laboratory coordinates *x, y, z*. Grey: scattering plane. Incoming beam (grey, from left) is diffracted by scattering angle 2θ, with scattering vector (blue) inclined by tilt angle $\psi = \theta$ to the load axis, *z*. Diffracted beam (grey) and scattering vector have azimuthal angle β. Also indicated is the angle γ, as used in Eq. (2). (B) Grey-scale coded diffraction pattern on the 2D detector. Innermost ring is the Au(111) reflection. Specimen NC_{60} in initial state (left) and after macroscopic compression strain of 8.5% (right).

In the diffraction geometry of this *in situ* experiment, the reflections at the azimuthal pattern angles $\beta = 90°, 270°$ belong to lattice plane normal tilted against the loading axis z by an angle ψ with $\psi = \pm\theta$ (θ = Bragg angle) and coplanar with the *y-z* plane of the specimen coordinates (c.f. Fig. 1(A)). In a first evaluation step powder diffraction patterns $I(\theta)$ were obtained by integration of the intensities over azimuthal sectors at $\beta \pm 15°$. The elastic strain $\varepsilon_\psi(\beta)$ in the direction of the reflection lattice plane normal is given by [19]

$$\varepsilon_\psi(\beta) = \frac{d(\beta) - d_0(\beta)}{d_0(\beta)} = \frac{sin\theta_0(\beta)}{sin\theta(\beta)} - 1, \quad (1)$$

where d_0 and d are the lattice spacings at a reference state and during the compression test, respectively. The Bragg angles, θ_0, θ, were obtained as maxima positions by fitting the sector-averaged diffraction data with Pseudo Voigt functions. Each of the ε_ψ with $\psi \equiv \{hkl\} = \{111\}$, $\{200\}$, $\{220\}$, $\{113\}$ and $\{222\}$ was evaluated as a function of the external stress and for each of the two azimuthal directions $\beta = 90°, 270°$.

The evaluation of the local stresses used the assumptions of 1) random texture and 2) applicability of Hooke's law with an averaging of the elastic constants after Reuss, see below, for the elastomechanics of the metal. We further assume that the local elastic strain state in specimen coordinates is completely specified by the transverse strain components ε_{xx}, ε_{yy} and the component, ε_{zz}, in the load direction. It then follows that the local strain, ε_ψ^{Loc}, in the direction of the scattering vector $\langle hkl \rangle$ is [19]

$$\varepsilon_\psi^{Loc} = \varepsilon_{xx}\,\sin^2\psi cos^2\gamma + \varepsilon_{yy}\sin^2\psi\sin^2\gamma + \varepsilon_{zz}\,cos^2\psi \quad (2)$$

Here ψ and γ are the polar and azimuthal angles, in the laboratory coordinates, of the direction $\langle hkl \rangle$ (see Fig. 1(A)).

The local stress state can be assumed uniaxial in *z*-direction. Then, for each crystallite contributing to a reflection in the direction $\beta = 90°, 270°$ (*i.e.* $\gamma = 90°$), Hooke's law implies

$$\varepsilon_\psi^{Loc}(\gamma = 90°) = \left(\boldsymbol{S}_{23} sin^2\psi + \boldsymbol{S}_{33} cos^2\psi\right)\sigma_{zz}, \quad (3)$$

Where the S_{ij} are entries of the compliance tensor, in laboratory coordinates, of that crystallite. For an fcc polycrystal the stress σ_{zz}^{Reuss} after Reuss can then be obtained from the mean of the local elastic strains, ε_ψ, by an averaging of the elastic compliances over all possible transformations with $\angle(\langle hkl \rangle, z) = \psi$,

$$\varepsilon_\psi(\beta = 90°, 270°) = \left(\langle \boldsymbol{S} \rangle_{23} sin^2\psi + \langle \boldsymbol{S} \rangle_{33} cos^2\psi\right)\sigma_{zz}^{Reuss} \quad (4)$$

The mean values of the tensors, *C*, of the elastic compliance and the elastic stiffness satisfy [20]

$$\langle C_{P,T} \rangle = \frac{1}{2\pi}\int_{\omega=0}^{2\pi} Q_{K,P}(\omega) Q_{M,T}(\omega) C_{K,M}^{crys}, \quad (5)$$

$$\langle S \rangle = \left\langle C^{-1} \right\rangle \quad (6)$$

Here Voigt's notation is used for the elastic stiffness coefficient, with the Cartesian axis labelled by indices *K,M* in crystal coordinates and *P,T* in specimen coordinates, respectively. The sum convention applies. $Q(\omega)$ is the tensor which transforms the elastic single crystal constants C_{KM}^{crys} in base crystal coordinates to all systems whose *z*-axes lie on a cone with aperture angle $2\theta = 2\psi$ around the lattice plane normal $\langle hkl \rangle$. Values for C_{11}, C_{12}, C_{44} for gold were taken from Ref. [21].

Fig. 1(B) shows examples of scattering patterns from sample NC_{60} before and during compression arising from the diffraction by the Gold phase. The diffraction rings have a noticeable granularity, which

results from the limited number of diffracting crystals. Intensity maxima from individual crystals are spread out in azimuthal direction, with a variance of almost zero, which indicates mosaic spread in the crystals. After 8.5% strain, the spread is increased and now amounts to ±3°. This value is in the same range as observed for the orientation splitting of grains in a bulk polycrystalline aggregate at moderate plastic strains [22].

Fig. 2A shows the experimental effective macroscopic stress-strain graphs of the *in situ* experiments. The macroscopic yield stresses are seen to differ, 100 MPa for specimen NC_{60} and 76 MPa for NC_{200}. The stresses at 4% plastic strain are considered here as representative of a state, where both constituents have reached the plastic deformation. This plastic flow criterion is met at 114 MPa and 94 MPa for specimens NC_{60} and NC_{200}, respectively.

Fig. 2B shows four examples of the X-ray strains $\varepsilon_\psi(\beta = 90°, 270°)$ for either one of the two specimens, plotted *versus* the macroscopic stress. All X-ray strains are referred to the projected lattice parameters at zero load in the respective orientation. Graphs such as Fig. 2B were found initially linear and in close but not perfect agreement for opposing β.

After the onset of plasticity, a splitting of the strain-stress graphs of the azimuthal angles β = 90°, 270 was observed for almost all reflections. This can be explained as follows: For a polycrystal with random texture and a statistically representative number of irradiated crystallites in the irradiated volume both cases β = 90°, 270° should be equivalent. However this is not the case for the investigated specimens, where the number of crystallites in the irradiated volume is below 100 and the number of crystallites contributing to any specific reflection {hkl} even lower. Since each reflection from a polycrystal under stress is influenced by the local stress state of diffraction volume, statistical scatter arises from averaging over few grains from different ensembles. Further variation results from the strong absorption in Au, which leads to different absorption for different x-ray pathways through the sample. In the interest of a representative analysis, we restrict the discussion to results obtained by averaging over opposed azimuthal angles.

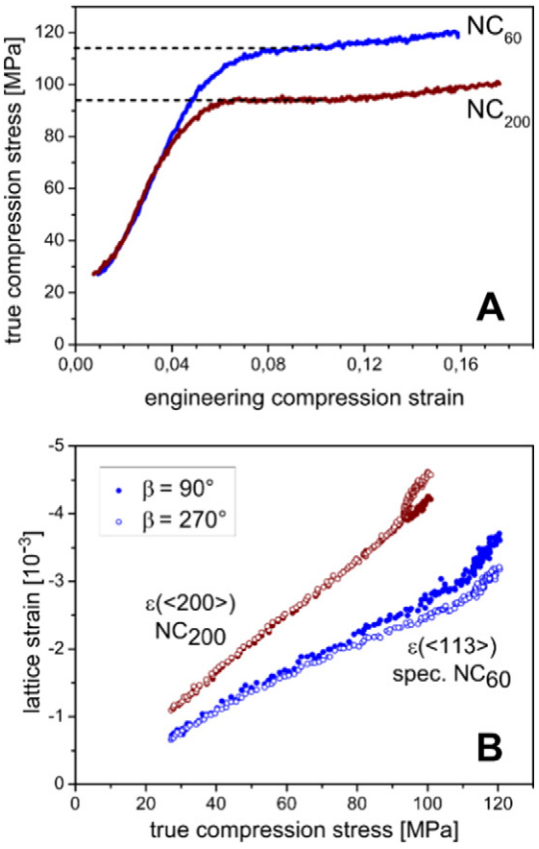

Fig. 2. Stress-strain relations from *in situ* compression tests of two composites with ligament sizes 60 nm (NC_{60}) and 200 nm (NC_{200}). **A** True effective macroscopic compression stress *versus* engineering strain. Stresses at 4% plastic strain are denoted by horizontal lines. B Lattice strains ε_ψ for the directions ⟨113⟩ (for NC_{60}) and ⟨200⟩ (for NC_{200}) evaluated from the azimuthal directions β = 90° and 270°.

From each single value of the X-ray strain the Reuss average of the microscopic stress was calculated after Eqs. (2)–(6). The resulting Reuss micro- *vs.* macrostress curves for the reflections {200}, {220}, {110} and {222} are shown in Fig. 3. The stress curves exhibit a good consistency for all measured reflections. This supports the Reuss averaging as well as the microscopic stress values of our study. Using again the 4% strain state as representative for stable plastic flow of both constituents in the composite, we find flow stresses in the metal phase of $\sigma_{zz}^{metal} = 193 \pm 11$ MPa for NC_{60} and $\sigma_{zz}^{metal} = 169 \pm 16$ MPa for NC_{200}.

The key findings of our study are values for the strength or, more appropriately, the flow stresses at an early stage of the plastic deformation. The macroscopic behavior, as measured by the load cell, is representative of averages of the stresses in the phases of the composite. In addition, the lattice parameter data directly measure averages of the local stresses in the nanoscale metal ligaments. Since the experiment probes plastic flow *in situ*, the stresses directly monitor the flow stress of a nanoscale metal. We now discuss the implications for the mechanical behavior of the metal and for the load partitioning in the composite.

Reference [10] has compiled previous results for the local strength at the ligament level derived from tests on mm-scale NPG or NPG-based composites. Fig. 4 compares our results to that earlier data. The most obvious observation is that the local flow stress of our 60 nm material agrees precisely with the previous reports for NPG and for composite samples. This is remarkable in particular since the earlier NPG data was partly inferred from macroscopic tests, assuming that the Gibson Ashby scaling relation holds. Recall that the present data is directly measured from the lattice parameters, without assumptions on effective stress averaging in a network that underlies the scaling relation. The agreement therefore supports the earlier analysis and specifically its assumption that the Gibson Ashby relation is in fact applicable to NPG. This would seem to argue against an anomalously low connectivity in the network, which has been speculated upon [10,17] in view of the rather low yield strength.

Focusing first on the sample with the smallest ligament size, NC_{60}, we emphasize the excellent agreement of our result for the local strength with the previous data. This means that the local flow stress in the metal has now been consistently measured by three independent approaches, emphasizing the consistency of the underlying pictures, and specifically supporting the high-strength of the metal ligaments at small size, similar to what has been found for isolated nano-objects.

With attention to Fig. 4 we note that, contrary to the 60 nm sample, the one with 200 nm ligament size is considerably stronger than inferred from the earlier experiments on pure NPG. This confirms a trend that already emerged in the earlier results from a model based evaluation of macroscopic flow stress data of NPG-based composites [9]. By comparing our NC_{200} data to the much lesser strength inferred from combining NPG data with Gibson Ashby scaling, one is lead to speculate on a failure of the Gibson Ashby model to describe the behavior of the NPG (in earlier publications) at larger L. This would seem to contradict our above conclusions. Yet, the observation is consistent with the proposition, in Ref. [10], that ligament growth during annealing (here from 60 to 200 nm) may reduce the scaled network connectivity, similar to what happens during the percolation-to-cluster transition in late-stage spinodal coarsening. With a poorly connected ligament network in the 200 nm sample, the Gibson Ashby relations would be less suitable for describing the load distribution in the metal network.

Owing to its microstructural heterogeneity, such as disorder in the network structure and a distribution of ligament cross-sections, NPG under load exhibits a wide distribution of local stresses [23,24]. As is common in heterogeneous media, the experiment then probes an

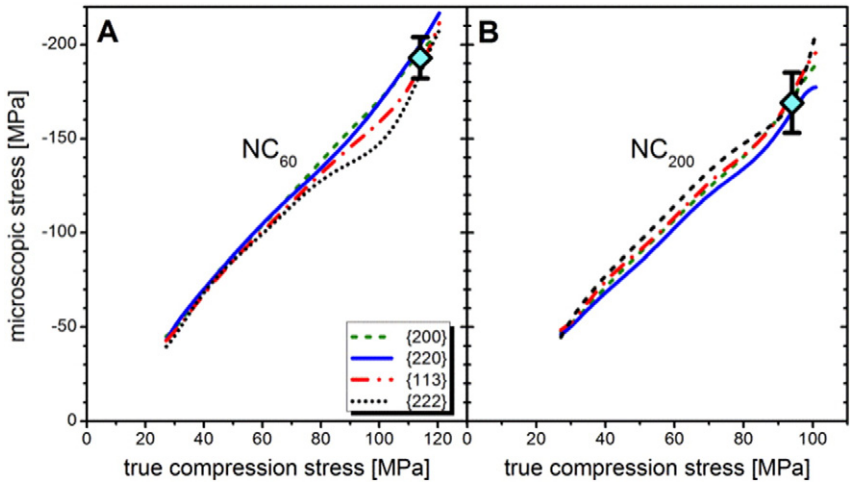

Fig. 3. Microscopic stresses in the gold crystal lattice *vs.* true compression stresses for specimens NC_{60} (A) and NC_{200} (B). Curves are best nonlinear regression fits to point clouds of Reuss stresses from four different reflections. Symbols: microscopic stress at 4% macroscopic plastic strain.

effective yield stress which differs from the local stress in that part of the microstructure where plasticity is initiated. Stress distribution is accounted for by models, such as the Gibson-Ashby approach, where networks of struts exhibit a mixed stress state, compression/tension as well as bending. Bending has been identified as the dominant deformation mode of the ligaments in NPG [25]. This is of relevance for deformation studies on NPG in general, and specifically for *in situ* diffraction studies under load, since the mean lattice parameter is poorly sensitive to bending. Yet, infiltrating the porous metal with a polymer changes the plastic flow field by enhancing the tension/compression component [8,9], which is reflected in the diffraction data. Thus, the lattice parameter variations in our study of nanocomposites will indeed correlate with the local yield stress. This notion is supported by our finding of a good agreement between the diffraction-based yield stress and data inferred from compression tests.

In our experiments the lattice-parameter based data for the local stress in the metal phase is supplemented by data for the effective macroscopic stress in the composite, provided by a load cell. We now discuss the implications for the partitioning of the stresses between metal- and polymer-phase of the composites. The partition of stresses must satisfy [26]

$$\sigma_{zz}^{macro} = \varphi\,\sigma_{zz}^{metal} + (1-\varphi)\sigma_{zz,}^{polymer} \tag{7}$$

where the σ_{zz} are the stresses in load direction, averaged either macroscopically or in each of the two components. For the present materials, the stress of the polymer phase at 4% plastic strain, as calculated after Eq. 7, amounts to 81 ± 5 MPa and 40 ± 11 MPa for the specimens NC_{60} and NC_{200} respectively. This difference may suggest that the flow stress of the polymer increases with decreasing pore size.

To summarize, this work studied the stress distribution in an interpenetrating-phase NPG-based nanocomposite material by *in situ* x-ray diffraction during compressive plastic flow. At small structure size we find excellent agreement with previous reports, supporting the match between material and model of those studies. Yet, deviations at larger structure size are compatible with the suggestion from previous work, that coarsening changes the connectivity in the metal network structure, an effect which is ignored by standard models.

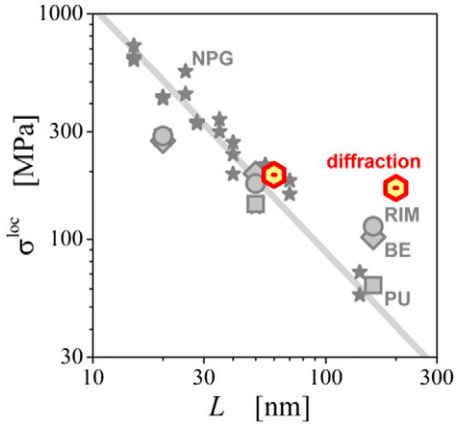

Fig. 4. Local flow stress, σ^{loc}, at 4% macroscopic plastic strain in the metal phase *versus* ligament size L. Comparison of direct, diffraction derived data (colored hexagons) to literature values inferred from experimental macroscopic flow stress and micromechanical theory linking macroscopic and microscopic stresses. Published data for similar, nanoporous gold- (NPG-) type materials are from the compilation in Ref. [10]: stars, NPG analyzed with the Gibson-Ashby scaling law. Large grey symbols, NPG-based composite materials with the polymers RIM, BE, PU, evaluated with the linear mixing rule of Ref. [9]. Line: $\sigma^{loc} \propto L^{-1}$, see Ref. [10].

Acknowledgements

Bernd Schwebke and Rainer Behn supported the measurement and data analysis. Financial support from DFG *via* SFB 986 "Tailor-Made Multiscale Materials Systems - M^3", subprojects B2 and Z2, is acknowledged.

References

[1] A.M. Hodge, J. Biener, J.R. Hayes, P.M. Bythrow, C.A. Volkert, A.V. Hamza, Acta Mater. 55 (2007) 1343–1349.
[2] H.J. Jin, L. Kurmanaeva, J. Schmauch, H. Rosner, Y. Ivanisenko, J. Weissmüller, Acta Mater. 57 (2009) 2665–2672.
[3] H.J. Jin, J. Weissmüller, Science 332 (2011) 1179–1182.
[4] M.D. Uchic, D.M. Dimiduk, J.N. Florando, W.D. Nix, Science 305 (2004) 986–989.
[5] J.R. Greer, W.C. Oliver, W.D. Nix, Acta Mater. 53 (2005) 1821–1830.
[6] C.A. Volkert, E.T. Lilleodden, D. Kramer, J. Weissmüller, Appl. Phys. Lett. 89 (2006) 061920.
[7] J.R. Greer, J.T.M. De Hosson, Prog. Mater. Sci. 56 (2011) 654–724.
[8] K. Wang, J. Weissmüller, Adv. Mater. 25 (2013) 1280–1284.
[9] K. Wang, A. Kobler, C. Kübel, H. Jelitto, G. Schneider, J. Weissmüller, NPG Asia Mater. 7 (2015), e187.
[10] N. Mameka, K. Wang, J. Markmann, E.T. Lilleodden, J. Weissmüller, Mater. Res. Lett. 4 (2016) 27–36.
[11] J. Biener, A.M. Hodge, J.R. Hayes, C.A. Volkert, L.A. Zepeda-Ruiz, A.V. Hamza, F.F. Abraham, Nano Lett. 6 (2006) 2379–2382.
[12] J. Biener, A.M. Hodge, A.V. Hamza, L.M. Hsiung, J.H. Satcher, J. Appl. Phys. 97 (2005) 024301.

[13] D. Lee, X. Wei, X. Chen, M. Zhao, S.C. Jun, J. Hone, E.G. Herbert, W.C. Oliver, J.W. Kysar, Scr. Mater. 56 (2007) 437–440.
[14] Y. Sun, J. Ye, Z. Shan, A.M. Minor, T.J. Balk, JOM 59 (2007) 54–58.
[15] T.J. Balk, C. Eberl, Y. Sun, K.J. Hemker, D.S. Gianola, JOM 61 (2009) 26–31.
[16] L.J. Gibson, M.F. Ashby, in: 2nd Edition ed. (Ed.), Cellular Solids: Structure and Properties, Pergamon Press, Oxford, 1999.
[17] X.-L. Ye, H.-J. Jin, Adv. Eng. Mater. 18 (2016) 1050–1058.
[18] N. Schell, A. King, F. Beckmann, H.U. Ruhnau, R. Kirchhof, R. Kiehn, M. Müller, A. Schreyer, AIP Conf. Proc. 1234 (2010) 391–394.
[19] V. Hauk, Structural and Residual Stress Analysis by Nondestructive Methods, Elsevier Science B.V, Amsterdam, 1997.
[20] C. Teodosiu, Elastic Models of Crystal Defects, Springer, Berlin Heidelberg, 1982.
[21] J.S. Blakemore, Solid State Physics, W. B. Saunders Company, 1969.
[22] R. Pokharel, J. Lind, A.K. Kanjarla, R.A. Lebensohn, S.F. Li, P. Kenesei, R.M. Suter, A.D. Rollett, Annu. Rev. Condens. Matter Phys. 5 (2014) 317–346.
[23] D. Farkas, A. Caro, E. Bringa, D. Crowson, Acta Mater. 61 (2013) 3249–3256.
[24] B.-N.D. Ngô, A. Stukowski, N. Mameka, J. Markmann, K. Albe, J. Weissmüller, Acta Mater. 93 (2015) 144–155.
[25] N. Huber, R.N. Viswanath, N. Mameka, J. Markmann, J. Weissmüller, Acta Mater. 67 (2014) 252–265.
[26] R. Hill, J. Mech, Phys. Solids 15 (1967) 79–95.